The Astrophysical Journal, 875:56 (11pp), 2019 April 10 https://doi.org/10.3847/1538-4357/ab0e7e

Toward Precision Tests of General Relativity with Black Hole X-Ray Reflection Spectroscopy

Ashutosh Tripathi[1], Sourabh Nampalliwar[2], Askar B. Abdikamalov[1], Dimitry Ayzenberg[1], Cosimo Bambi[1], Thomas Dauser[3], Javier A. García[3,4], and Andrea Marinucci[5]

[1] Center for Field Theory and Particle Physics and Department of Physics, Fudan University, 200438 Shanghai, People's Republic of China; bambi@fudan.edu.cn
[2] Theoretical Astrophysics, Eberhard-Karls Universität Tübingen, D-72076 Tübingen, Germany
[3] Remeis Observatory & ECAP, Universität Erlangen-Nürnberg, D-96049 Bamberg, Germany
[4] Cahill Center for Astronomy and Astrophysics, California Institute of Technology, Pasadena, CA 91125, USA
[5] Dipartimento di Matematica e Fisica, Universitá degli Studi Roma Tre, I-00146 Roma, Italy
Received 2018 November 23; revised 2019 March 8; accepted 2019 March 8; published 2019 April 16

Abstract

Astrophysical black hole systems are the ideal laboratories for testing Einstein's theory of gravity in the strong field regime. We have recently developed a framework that uses the reflection spectrum of black hole systems to perform precision tests of general relativity by testing the Kerr black hole hypothesis. In this paper, we analyze *XMM-Newton* and *NuSTAR* observations of the supermassive black hole in the Seyfert 1 galaxy MCG–06–30–15 with our disk reflection model. We consider the Johannsen metric with the deformation parameters α_{13} and α_{22}, which quantify deviations from the Kerr metric. For $\alpha_{22} = 0$, we obtain the black hole spin $0.928 < a_* < 0.983$ and $-0.44 < \alpha_{13} < 0.15$. For $\alpha_{13} = 0$, we obtain $0.885 < a_* < 0.987$ and $-0.12 < \alpha_{22} < 1.05$. The Kerr solution is recovered for $\alpha_{13} = \alpha_{22} = 0$. Thus, our results include the Kerr solution within statistical uncertainties. Systematic uncertainties are difficult to account for, and we discuss some issues in this regard.

Key words: accretion, accretion disks – black hole physics – gravitation

1. Introduction

Einstein's gravity has been extensively tested in the weak field regime, its theoretical predictions being largely confirmed by experiments in the solar system and radio observations of binary pulsars (Will 2014). The strong field regime, on the other hand, is still largely unexplored. There are many alternative and modified theories of gravity that have the same predictions as Einstein's gravity for weak fields and present deviations only when gravity becomes strong. Astrophysical black holes give us an opportunity to test the predictions of Einstein's gravity in the strong field regime (Bambi et al. 2016; Cardoso & Gualtieri 2016; Johannsen 2016; Yagi & Stein 2016; Bambi 2017; Krawczynski 2018).

In four-dimensional Einstein's gravity, the only stationary and asymptotically flat vacuum black hole solution, which is regular on and outside of the event horizon, is the Kerr metric (Carter 1971; Robinson 1975; Chruściel et al. 2012). The spacetime around astrophysical black holes is thought to be well approximated by this solution. Testing the Kerr black hole hypothesis with astrophysical black holes is thus a test of Einstein's gravity in the strong field regime, and can be seen as the counterpart of solar system experiments aimed at verifying the Schwarzschild solution in order to test Einstein's gravity in the weak field regime (Johannsen & Psaltis 2011, 2013; Bambi 2012a, 2012b, 2012c, 2013; Krawczynski 2012; Kong et al. 2014; Hoormann et al. 2016).

In this work, we study the X-ray spectrum of the supermassive black hole in MCG–06–30–15 with the reflection model RELXILL_NK (Bambi et al. 2017) as a step in our program to test the Kerr black hole hypothesis from the reflection spectrum of the disk of accreting black holes (Cao et al. 2018; Choudhury et al. 2018; Tripathi et al. 2018; Wang-Ji et al. 2018; Xu et al. 2018). MCG–06–30–15 is a very bright Seyfert 1 galaxy and it has been observed for many years by different X-ray missions. It is the source in which a relativistically blurred iron Kα line was clearly detected for the first time (Tanaka et al. 1995), and is thus one of the natural candidates for tests of Einstein's gravity using X-ray reflection spectroscopy. We analyze simultaneous observations of *XMM-Newton* (Jansen et al. 2001) and *NuSTAR* (Harrison et al. 2013), which provide both high energy resolution at the iron line (with *XMM-Newton*) and a broad energy band (with *NuSTAR*).

The contents of the paper are as follows. In Section 2, we briefly review the parameterized metric employed in our test and our previous results. In Sections 3 and 4 we present, respectively, our data reduction and analysis. Section 5 is devoted to the discussion of our results and the conclusions. Throughout the paper, we adopt the convention $G_{\rm N} = c = 1$ and a metric with signature $(-+++)$.

2. The Reflection Model RELXILL_NK

RELXILL_NK (Bambi et al. 2017) is the natural extension of RELXILL (Dauser et al. 2013; García et al. 2014) to non-Kerr spacetimes. It describes the disk's reflection spectrum of an accreting black hole (Bambi 2018). Here we employ the Johannsen metric. In Boyer–Lindquist-like coordinates, the line element reads (Johannsen 2013)

$$\begin{aligned} ds^2 = &-\frac{\tilde{\Sigma}(\Delta - a^2 A_2^2 \sin^2\theta)}{B^2} dt^2 + \frac{\tilde{\Sigma}}{\Delta A_5} dr^2 + \tilde{\Sigma} d\theta^2 \\ &- \frac{2a[(r^2+a^2)A_1 A_2 - \Delta]\tilde{\Sigma}\sin^2\theta}{B^2} dt d\phi \\ &+ \frac{[(r^2+a^2)^2 A_1^2 - a^2\Delta\sin^2\theta]\tilde{\Sigma}\sin^2\theta}{B^2} d\phi^2, \end{aligned} \quad (1)$$

Table 1
List of the Observations Analyzed in This Work

Mission	Observation ID	Exposure (ks)
NuSTAR	60001047002	23
	60001047003	127
	60001047005	30
XMM-Newton	0693781201	134
	0693781301	134
	0693781401	49

where M is the black hole mass, $a = J/M$, J is the black hole spin angular momentum, $\tilde{\Sigma} = \Sigma + f$, and

$$\Sigma = r^2 + a^2\cos^2\theta, \qquad \Delta = r^2 - 2Mr + a^2,$$
$$B = (r^2 + a^2)A_1 - a^2A_2\sin^2\theta. \tag{2}$$

The functions A_1, A_2, A_5, and f are

$$A_1 = 1 + \sum_{n=3}^{\infty}\alpha_{1n}\left(\frac{M}{r}\right)^n, \quad A_2 = 1 + \sum_{n=2}^{\infty}\alpha_{2n}\left(\frac{M}{r}\right)^n,$$
$$A_5 = 1 + \sum_{n=2}^{\infty}\alpha_{5n}\left(\frac{M}{r}\right)^n, \quad f = \sum_{n=3}^{\infty}\epsilon_n\frac{M^n}{r^{n-2}}. \tag{3}$$

The "deformation parameters" $\{\alpha_{1n}\}$, $\{\alpha_{2n}\}$, $\{\alpha_{5n}\}$, and $\{\epsilon_n\}$ are used to quantify possible deviations from the Kerr background. In what follows, we restrict our attention to the deformation parameters α_{13} and α_{22}, since these two have the strongest impact on the reflection spectrum (Bambi et al. 2017). In our analysis, we leave either one of α_{13} and α_{22} free, setting the other to zero. All other deformation parameters are set identically to zero. In order to avoid spacetimes with pathological properties, we require $|a_*| \leqslant 1$, where $a_* = a/M = J/M^2$ is the dimensionless spin parameter, and (Tripathi et al. 2018)

$$-(1 + \sqrt{1 - a_*^2})^2 < \alpha_{22} < \frac{(1 + \sqrt{1 - a_*^2})^4}{a_*^2},$$
$$\alpha_{13} > -\frac{1}{2}(1 + \sqrt{1 - a_*^2})^4. \tag{4}$$

From the analysis of the reflection spectrum of astrophysical black holes with RELXILL_NK we can constrain the deformation parameters α_{13} and α_{22} and check whether they are consistent with zero, as required by the Kerr black hole hypothesis. In Cao et al. (2018), we analyzed *XMM-Newton*, *NuSTAR*, and *Swift* data of the supermassive black hole in 1H0707–495 and we got the first constraint of α_{13} (see Bambi et al. 2018 for the same constraints with an updated version of RELXILL_NK). In Tripathi et al. (2018) and Choudhury et al. (2018), we analyzed *Suzaku* data of, respectively, the supermassive black hole in Ark 564 and Mrk 335, and we constrained the deformation parameters α_{13} and α_{22}. In Wang-Ji et al. (2018) and Xu et al. (2018), we tested the Kerr nature of the stellar-mass black holes in GX 339–4 and GS 1354–645, respectively.

For these five sources, three supermassive black holes and two stellar-mass black holes, we have found that the value of the deformation parameters is consistent with zero at least within a 90% confidence level (and usually within 68% confidence level). The most stringent constraints have been obtained from GS 1354–645, where the bounds on a_*, α_{13}, and α_{22} are (99% of confidence level for two relevant parameters)

$$a_* > 0.975 \quad -0.34 < \alpha_{13} < 0.16 \quad (\text{for } \alpha_{22} = 0), \tag{5}$$

$$a_* > 0.975 \quad -0.09 < \alpha_{22} < 0.42 \quad (\text{for } \alpha_{13} = 0). \tag{6}$$

Our results are thus consistent with the Kerr black hole hypothesis, as expected. However, these results were not obvious a priori considering the possible systematic effects of our model, which are not fully under control. This, in turn, might be interpreted as the fact that the systematic uncertainties are subdominant for the current precision of our tests.

3. Observations and Data Reduction

MCG–06–30–15 is a very bright Seyfert 1 galaxy at redshift $z = 0.007749$ with many observations from different X-ray missions; see, for instance, Iwasawa et al. (1996), Guainazzi et al. (1999), Lee et al. (2001), Wilms et al. (2001), Fabian et al. (2002), Brenneman & Reynolds (2006), Miniutti et al. (2007), Miller et al. (2008), and Marinucci et al. (2014). This source has a broad and very prominent iron Kα line, so it is quite a natural candidate for our tests of the Kerr metric using X-ray reflection spectroscopy. However, the source is very variable, which requires some attention in the data analysis.

NuSTAR and *XMM-Newton* observed MCG–06–30–15 simultaneously starting on 2013 January 29 for a total time of ∼360 ks and ∼315 ks, respectively. Table 1 shows the observation ID and their exposure time. A study of these data was reported in Marinucci et al. (2014).

NuSTAR is comprised of two coaligned telescopes with focal plane modules (FPMA and FPMB; Harrison et al. 2013). The level 1 data products are analyzed using NuSTAR Data Analysis Software (NUSTARDAS). The downloaded raw data are converted into event files (level 2 products) using the HEASOFT task NUPIPELINE and using the latest calibration data files taken from NuSTAR calibration database (CALDB) version 20180312. The size of the source region is taken to be 70 arcsec centered at the source and that of the background is 100 arcsec taken from the same CCD. The final products (light curves, spectra) are extracted using the event files and region files by running the NUPRODUCTS task. Spectra are rebinned to 70 counts per bin in order to apply χ^2 statistics.

For *XMM-Newton*, observations from three consecutive revolutions are taken with the two EPIC cameras Pn and MOS1/2 operating in medium filter and small window modes (Jansen et al. 2001). Here, we are only using Pn data owing to their better quality (Strüder et al. 2001). The MOS data are not used in our analysis because they suffered from high pile-up. SAS version 16.0.0 is used to convert the raw data into event files. These event files are then combined into a single fits file using ftool FMERGE. Good time intervals (GTIs) are generated using TABTIGEN and then used in filtering the event files. For source events, we take a circular region of 40 arcsec centered at the source. For background, we take a 50 arcsec region. After backscaling, response files are produced. Finally, in order to apply the χ^2 statistics, spectra are rebinned in order to oversample the instrumental resolution by at least a factor of 3 and have 50 counts in each background-subtracted bin.

Source and background spectra of each instrument are shown in Figure 1.

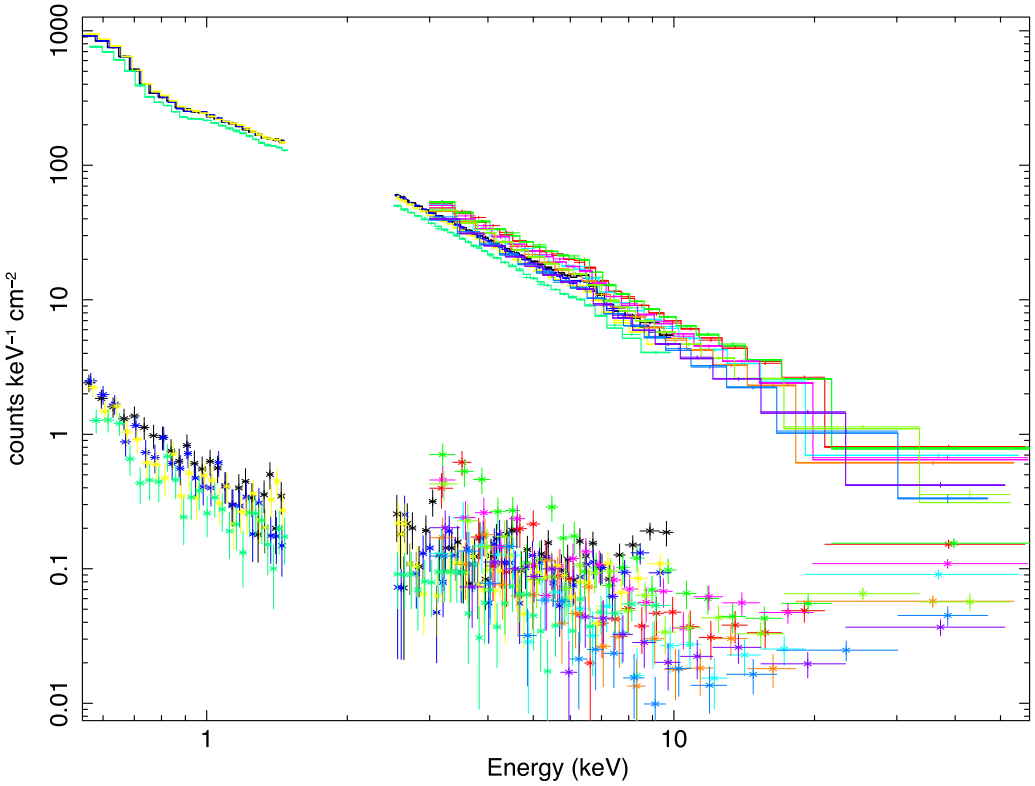

Figure 1. Source (the data in the upper part of the figure) and background (the data with the stars in the lower part of the figure) spectra for EPIC-Pn, FPMA, and FPMB for all the four flux states considered in this work. The data are divided by the response effective area of each particular channel.

As the source is highly variable, it is important to use simultaneous data so that variability is properly taken into account. We use ftool mgtime to find the common GTIs of the two telescopes.

4. Spectral Analysis

MCG–06–30–15 is highly variable in the X-ray band. This could be due to passing clouds near the black hole along our line of sight and/or variations of the coronal geometry, as both phenomena can have a timescale shorter than our observations. To take such a source variability into account, we have arranged our data into four groups according to the flux state of the source (low flux state, medium flux state, high flux state, and very high flux state). Since we have data from three instruments (*XMM-Newton*, *NuSTAR*/FPMA, and *NuSTAR*/FPMB), in the end we have to deal with 12 data sets. The data are divided into four flux states such that spectral data counts will be similar in each flux state as shown in Figure 2. Luminosities and fluxes in the energy range 0.5–10 keV for *XMM-Newton* and 3–80 keV for *NuSTAR* for every data set are shown in Table 2. Note that our grouping scheme is different from that employed in Marinucci et al. (2014), which was based on the hardness of the source.

To combine the *XMM-Newton* and *NuSTAR* data, we set the constant of *XMM-Newton* to 1 and we leave the constants of *NuSTAR*/FPMA and *NuSTAR*/FPMB free. After the fit, we check that the ratio between the constants of *NuSTAR*/FPMA and *NuSTAR*/FPMB is between 0.95 and 1.05. Table 3 shows the values of these constants for every flux state.

As discussed in the appendix of Marinucci et al. (2014), in the *XMM-Newton* data we see a spurious Gaussian around 2 keV. This is interpreted as an effect of the golden edge in the response file due to miscalibration in the long-term charge transfer inefficiency (CTI), i.e., how photon energies are reconstructed after detection. We solve this issue by simply ignoring the energy range 1.5–2.5 keV in the *XMM-Newton*/EPIC-Pn data. Such a region is not crucial for testing the Kerr metric and therefore its omission is not so important for the final result. We cannot add an ad hoc Gaussian to fit this feature because this would also modify the way in which the warm absorbers/ionized reflectors reproduce the data.

We can perform two kinds of analysis. We can fit the data of every flux state independently and thus get a measurement for every model parameter for every flux state (single-flux state analysis), or we can fit the four data groups together (multi-flux state analysis). In the latter case, some model parameters are allowed to change value from a flux state to another one, and other parameters must be constant over different flux states. The multi-flux state analysis can usually provide more precise measurements of the model parameters, because of the higher photon statistics, and represents our "final" result. Here we also report the results of our single-flux state analysis to show that the corresponding measurements of the deformation parameters are consistent with the measurements of the multi-flux state analysis for every flux state.

We first try to fit the data of the low flux state with a simple power law to identify the spectral features. The notable features above 3 keV are the iron Kα line around 6.4 keV and the Compton hump at 20–30 keV (see Figure 3; George & Fabian 1991; Ross & Fabian 2005). Below 3 keV, there are features from complex ionized absorbers (Lee et al. 2001; Sako et al. 2003). In Lee et al. (2000), the authors studied the low energy spectrum of this source and found that fitting requires two warm absorbers and one neutral absorber; this is the choice

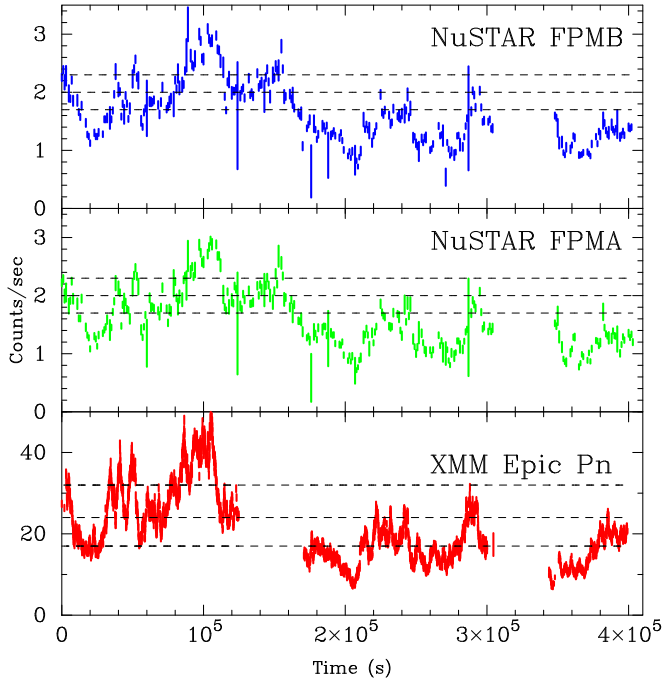

Figure 2. *NuSTAR*/FPMA, *NuSTAR*/FPMB, and *XMM-Newton*/EPIC-Pn light curves. The three dashed horizontal lines separate the four different flux states.

Table 2
Average Luminosity (Assuming $z = 0.007749$) and Average Photon Flux in the Energy Range 0.5–10 keV for *XMM-Newton* and 3–80 keV for *NuSTAR* for Every Flux State and Instrument

	Luminosity (10^{43} erg s^{-1})				Flux (10^{-10} erg cm^{-2} s^{-1})			
Group	1	2	3	4	1	2	3	4
XMM-Newton	0.59	0.83	1.12	1.54	0.44	0.62	0.84	1.15
NuSTAR/FPMA	1.01	1.24	1.50	2.03	0.76	0.93	1.12	1.53
NuSTAR/FPMB	1.04	1.27	1.52	2.07	0.78	0.95	1.14	1.55

Note. Group 1 is for the low flux state, group 2 is for the medium flux state, group 3 is for the high flux state, and group 4 is for the very high flux state.

Table 3
Cross Calibration Constants between *XMM-Newton* and *NuSTAR*

Group	1	2	3	4
XMM-Newton	1	1	1	1
NuSTAR/FPMA	1.060	1.044	1.043	1.053
NuSTAR/FPMB	1.089	1.065	1.058	1.072

Note. The constant of *XMM-Newton* is frozen to 1.

extensively adopted in the literature (Brenneman & Reynolds 2006; Marinucci et al. 2014). In order to fit the spectrum, we employ the model consisting of the following components: nonrelativistic reflection from distant cold material, relativistic reflection from the ionized accretion disk, and power law for primary emission. We use XILLVER for the cold reflection (García & Kallman 2010; García et al. 2011, 2013), RELXILL_NK for the blurred reflection (Bambi et al. 2017), and CUTOFFPL for the power-law emission with free cutoff

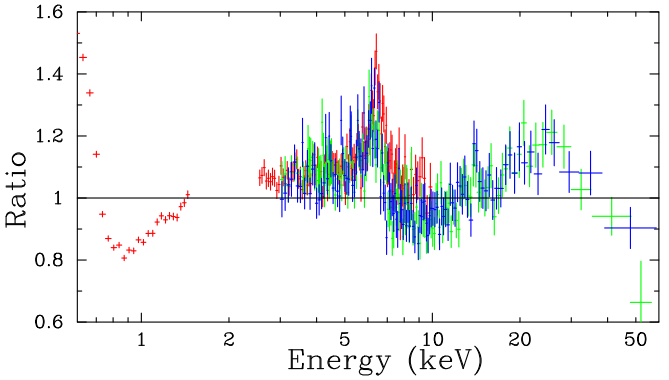

Figure 3. Data to best-fit model ratio for the model TBABS × CUTOFFPL for the low flux state. We can clearly see the reflection features of the spectrum: broad iron line around 6 keV, Compton hump around 20 keV, and soft excess below 1 keV. Red crosses are used for *XMM-Newton*, green crosses for *NuSTAR*/FPMA, and blue crosses for *NuSTAR*/FPMB.

Table 4
Statistics of the Best-fit Models in the Multi-flux State Analysis

Model	χ^2	ν	χ^2/ν
0	47319	2727	17.35
1	18994	2726	6.9677
2	11196	2718	4.1192
3	10801	2711	3.9841
4	10674	2702	3.9504
5	3486.80	2691	1.29573
6	3384.89	2689	1.25879
7	3094.98	2688	1.15141
8	3029.10	2685	1.12816

Note. Model 0 is TBABS × CUTOFFPL. In model 1, we add DUSTYABS to model 0. In Models 2, 3, and 4, we add, respectively, one, two, and three WARMABS to model 1. In model 5, we add RELXILL_NK to model 3. In model 6, we add XILLVER to model 5. In model 7 and 8, we add one and two ZGAUSS, respectively, to model 6.

energy. A narrow emission line and a narrow absorption line are also required. The combination of the abovementioned models is convolved with two ionized absorbers, one dusty absorber, and Galactic absorption as mentioned in the literature (Lee et al. 2000; Brenneman & Reynolds 2006; Marinucci et al. 2014). Table 4 shows the improvement of the fit as we add new components to the model for the multi-flux state analysis.

The final XSPEC model is TBABS × WARMABS$_1$ × WARMABS$_2$ × DUSTYABS ×(CUTOFFPL + RELXILL_NK + XILLVER + ZGAUSS + ZGAUSS). TBABS describes the Galactic absorption and we set the column density $N_{\rm H} = 3.9 \cdot 10^{20}$ cm^{-2} (Dickey & Lockman 1990). WARMABS$_1$ and WARMABS$_2$ are two ionized absorbers and their tables are generated with XSTAR v 2.41. DUSTYABS is a neutral absorber that modifies the soft X-ray band due to the presence of dust around the source (Lee et al. 2000). CUTOFFPL is a power law with an exponential cutoff and describes the direct radiation from the Comptonized corona. RELXILL_NK is our disk's reflection model for the Johannsen spacetime (Bambi et al. 2017), where the reflection fraction parameter is set to -1, so there is no power law from the corona because we prefer to use CUTOFFPL. XILLVER is the reflection spectrum from some ionized nonrelativistic matter at larger distance (García et al. 2013). After fitting the data with all the abovementioned model components, there are features at low energies that can be fit

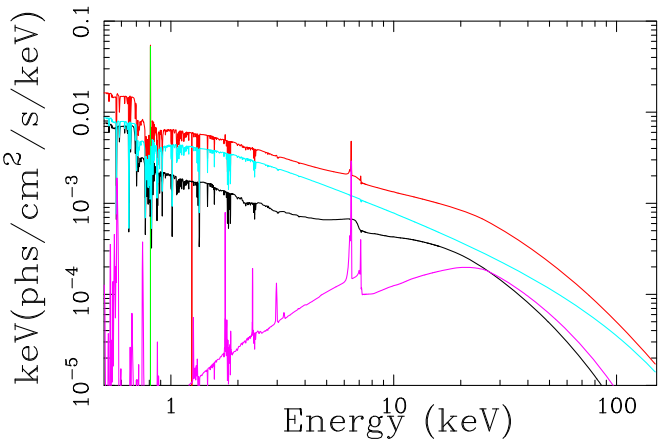

Figure 4. Spectrum of the best-fit of model *a* of the low flux state (red) and its components in the multi-flux state analysis: power-law component (blue), relativistic reflection component (black), nonrelativistic reflection component (magenta), and emission line (green).

with Gaussian profiles. One of the two ZGAUSS describes a narrow oxygen line around 0.81 keV and the other one describes a narrow absorption at 1.22 keV. The latter can be interpreted in terms of blueshifted oxygen absorption due to the presence of relativistic outflows (Leighly et al. 1997). The spectrum of the best-fit model with its components for the low flux state is shown in Figure 4.

We have two models: model *a* in which α_{13} is free and $\alpha_{22} = 0$, and model *b* where $\alpha_{13} = 0$ and α_{22} can vary. Thus, we test for one nonzero deformation parameter at a time. The best-fit values are reported in Table 5 (single-flux state analysis) and Table 6 (multi-flux state analysis) for both model *a* and model *b*. The estimated error is the 90% confidence interval for one parameter of interest ($\Delta\chi = 2.71$). From the comparison of Tables 5 and 6, we can see that the measurement of the deformation parameters in the single-flux state and multi-flux state analyses are consistent, which is what we should expect and validate our analysis method. In what follows, we will thus only focus on the results from the multi-flux state analysis, which provides more stringent constraints thanks to the higher photon statistics. Figure 5 shows the quality of our fits with the residuals for model *a* for the multi-flux state analysis (for model *b* we obtain very similar results).

In the multi-flux state analysis, some parameters are allowed to change value from one flux state to another one, while other parameters cannot. The column densities and the ionization parameters of the two warm absorbers are allowed to vary from different flux states. The neutral iron density in DUSTYABS is instead kept constant: it describes the absorption of the dust surrounding the source and its iron density should not change much among different flux states; see Lee et al. (2001) for more details about dust absorption in MCG–06–30–15. The photon index Γ and the energy cutoff $E_{\rm cut}$ to describe the spectrum of the corona are allowed to vary with the flux state because the geometry of the corona can change over the observational timescale.

For the disk's reflection spectrum described by RELXILL_NK, we start with an emissivity profile described by a broken power law and the inner emissivity index $q_{\rm in}$, the outer emissivity index $q_{\rm out}$, and the breaking radius $R_{\rm br}$ all free and allowed to vary with the flux state. However, we find that $q_{\rm out}$ is always consistent with 3, as we could expect in the case of a lamppost corona. For example, for model *a* we get $2.90^{+0.13}_{-0.12}$, $2.93^{+0.27}_{-0.19}$, $3.09^{+0.21}_{-0.16}$, and $2.78^{+0.28}_{-0.27}$ for the four flux states. We thus repeat the fit freezing $q_{\rm out}$ to 3. The inclination angle of the accretion disk, the black hole spin, the deformation parameters, and the iron abundances are clearly constant over the observation period. The ionization parameter ξ is allowed to vary because it is affected by the geometry of the corona, which may change at different flux states. The normalization also varies among different flux states. We freeze the reflection fraction of RELXILL_NK to be -1 so that it only returns the reflection component. The power-law component is modeled with CUTOFFPL and the cutoff energy is left free because it can be estimated from the *NuSTAR* data.

In XILLVER, the parameters are tied to those in RELXILL_NK, with the exception of the ionization and iron abundance. For the ionization parameter, we set $\log \xi' = 0$, as the nonrelativistic reflection component is thought to be produced far away from the black hole, in the outer part of the accretion disk or the molecular torus. The iron abundance is fixed at solar value as the distant cold reflector likely has a low iron abundance. The normalization is tied between different flux states as the distant reflector is not expected to vary much.

5. Discussion and Conclusions

The primary aim of this work is put constraints on possible deviations from the Kerr solution. For $\alpha_{22} = 0$, our constraints on the black hole spin parameter a_* and the Johannsen deformation parameter α_{13} are (99% confidence level for two relevant parameters)

$$0.928 < a_* < 0.983, \qquad -0.44 < \alpha_{13} < 0.15. \tag{7}$$

When we assume $\alpha_{13} = 0$, we find (still 99% confidence level for two relevant parameters)

$$0.885 < a_* < 0.987, \qquad -0.12 < \alpha_{22} < 1.05. \tag{8}$$

In both cases, the value of the deformation parameter is consistent with 0, which is the value required by the Kerr solution and predicted by Einstein's gravity. The confidence level contours a_* versus α_{13} and a_* versus α_{22} are shown in Figure 6 ($\Delta\chi^2 = 2.30$, 4.61, and 9.21 corresponding, respectively, to 68%, 90%, and 99% for two relevant parameters).

The Johannsen metric is a parametric black hole background, so it is not a solution of a specific theory of gravity and, in general, it is not possible to make predictions on the expected values of its deformation parameters. In such a context, it is also difficult to compare constraints from different sources, because there are theoretical models where deviations from the Kerr metric are independent of the black hole mass and other theoretical models in which deviations from standard predictions do depend on the black hole mass. In the latter case, the constraints obtained from stellar-mass black holes cannot be directly compared to those from supermassive black holes. The goal of tests of the Kerr solution with parametric black hole metrics is thus to get stronger and stronger constraints on the deformation parameters and check whether they are consistent with zero, as it is the case in a typical null-experiment. Bearing this in mind, we can note that the constraints on α_{13} and α_{22} inferred in the present work from the supermassive black hole in MCG–06–30–15 are the most stringent ones among those we have obtained so far from supermassive black holes and comparable only to those obtained from the stellar-mass black hole in GS 1354–645.

Table 5
Single-flux State Analysis

Model	*a*				*b*			
Group	1	2	3	4	1	2	3	4
TBABS								
$N_{\rm H}/10^{22}$ cm^{-2}	0.039[a]	0.039[a]	0.039[a]	0.039[a]	0.039[a]	0.039[a]	0.039[a]	0.039[a]
WARMABS$_1$								
$N_{\rm H1}/10^{22}$ cm^{-2}	$0.93^{+0.10}_{-0.08}$	$1.00^{+0.09}_{-0.08}$	$0.98^{+0.07}_{-0.14}$	$0.13^{+0.08}_{-0.12}$	$0.96^{+0.10}_{-0.11}$	$0.99^{+0.06}_{-0.09}$	$0.97^{+0.10}_{-0.11}$	$0.14^{+0.52}_{-0.09}$
$\log \xi_1$	$1.906^{+0.019}_{-0.013}$	$2.11^{+0.03}_{-0.04}$	$2.11^{+0.07}_{-0.03}$	$3.0^{+0.4}_{-0.4}$	$1.95^{+0.03}_{-0.05}$	$2.113^{+0.033}_{-0.015}$	$2.11^{+0.05}_{-0.09}$	$3.2^{+0.3}_{-0.3}$
WARMABS$_2$								
$N_{\rm H2}/10^{22}$ cm^{-2}	$0.7^{+0.3}_{-0.3}$	$0.9^{+0.7}_{-0.3}$	$1.2^{+0.5}_{-0.3}$	$0.83^{+0.08}_{-0.07}$	$0.7^{+0.4}_{-0.4}$	$0.9^{+0.7}_{-0.4}$	$1.1^{+0.5}_{-0.3}$	$0.82^{+0.03}_{-0.10}$
$\log \xi_2$	$3.20^{+0.06}_{-0.11}$	$3.30^{+0.10}_{-0.07}$	$3.31^{+0.07}_{-0.05}$	$2.03^{+0.15}_{-0.11}$	$3.22^{+0.07}_{-0.13}$	$3.30^{+0.10}_{-0.06}$	$3.31^{+0.07}_{-0.05}$	$2.04^{+0.04}_{-0.04}$
DUSTYABS								
$\log (N_{\rm Fe}/10^{21}$ cm$^{-2})$	$17.42^{+0.08}_{-0.06}$	$17.56^{+0.03}_{-0.06}$	$17.52^{+0.05}_{-0.06}$	$17.54^{+0.03}_{-0.07}$	$17.43^{+0.07}_{-0.09}$	$17.56^{+0.04}_{-0.06}$	$17.51^{+0.05}_{-0.05}$	$17.546^{+0.015}_{-0.050}$
CUTOFFPL								
Γ	$1.932^{+0.020}_{-0.020}$	$1.965^{+0.018}_{-0.021}$	$1.993^{+0.020}_{-0.008}$	$2.025^{+0.012}_{-0.015}$	$1.93^{+0.03}_{-0.03}$	$1.962^{+0.014}_{-0.011}$	$1.988^{+0.013}_{-0.018}$	$2.018^{+0.018}_{-0.037}$
$E_{\rm cut}$ [keV]	211^{+82}_{-39}	116^{+33}_{-21}	145^{+50}_{-36}	>193	201^{+94}_{-46}	113^{+37}_{-16}	145^{+48}_{-34}	290_{-101}
$N_{\rm CUTOFFPL}$ (10^{-3})	$7.1^{+1.7}_{-2.8}$	$13.3^{+1.6}_{-1.6}$	$15.4^{+1.4}_{-4.7}$	23^{+3}_{-6}	$7.1^{+1.6}_{-2.4}$	$13.3^{+0.6}_{-0.5}$	15^{+4}_{-4}	22^{+3}_{-6}
RELXILL_NK								
$q_{\rm in}$	$7.8^{+1.4}_{-1.4}$	$7.0^{+2.2}_{-1.4}$	$7.8^{+1.9}_{-1.4}$	>8.1	$7.9^{+1.1}_{-0.7}$	$7.1^{+1.9}_{-0.7}$	$7.7^{+1.8}_{-1.2}$	>9.2
$q_{\rm out}$	3[a]	3[a]	3[a]	3[a]	3[a]	3[a]	3[a]	3[a]
$R_{\rm br}$ $[M]$	$3.2^{+0.3}_{-0.6}$	$3.4^{+0.7}_{-1.0}$	$3.4^{+0.3}_{-0.4}$	$3.03^{+0.10}_{-0.18}$	$3.16^{+0.19}_{-0.70}$	$3.5^{+0.5}_{-0.4}$	$3.4^{+0.5}_{-0.3}$	$2.94^{+0.53}_{-0.11}$
i [deg]	29^{+3}_{-3}	31^{+3}_{-3}	29^{+3}_{-3}	36^{+3}_{-3}	$28.9^{+2.3}_{-2.4}$	31^{+3}_{-3}	29^{+3}_{-4}	36^{+4}_{-4}
a_*	>0.980	$0.99_{-0.04}$	$0.99_{-0.03}$	$0.982^{+0.006}_{-0.017}$	>0.95	>0.977	$0.99_{-0.03}$	$0.993_{-0.007}$
α_{13}	$0.0^{+0.2}_{-0.6}$	$0.0^{+0.2}_{-0.5}$	$0.15^{+0.14}_{-0.27}$	$0.2^{+0.2}_{-0.7}$	0[a]	0[a]	0[a]	0[a]
α_{22}	0[a]	0[a]	0[a]	0[a]	$-0.02^{+0.94}_{-0.11}$	$-0.12^{+1.29}_{-0.04}$	$-0.13^{+0.87}_{-0.04}$	$-0.18^{+0.62}_{-0.02}$
z	0.007749[a]	0.007749[a]	0.007749[a]	0.007749[a]	0.007749[a]	0.007749[a]	0.007749[a]	0.007749[a]
$\log \xi$	$3.031^{+0.018}_{-0.031}$	$3.000^{+0.025}_{-0.131}$	$3.07^{+0.05}_{-0.04}$	$3.11^{+0.07}_{-0.05}$	$3.035^{+0.025}_{-0.039}$	$3.000^{+0.022}_{-0.140}$	$3.08^{+0.04}_{-0.04}$	$3.13^{+0.05}_{-0.06}$
$A_{\rm Fe}$	$4.4^{+1.3}_{-1.5}$	>5.8	$4.2^{+3.2}_{-1.1}$	$3.9^{+0.6}_{-1.2}$	$4.7^{+2.9}_{-0.9}$	>4.8	$4.0^{+1.7}_{-0.8}$	$3.5^{+1.0}_{-0.7}$
$N_{\rm RELXILL\_NK}$ (10^{-3})	$0.254^{+0.068}_{-0.020}$	$0.23^{+0.09}_{-0.06}$	$0.29^{+0.15}_{-0.07}$	$0.28^{+0.13}_{-0.06}$	$0.26^{+0.10}_{-0.10}$	$0.22^{+0.04}_{-0.06}$	$0.30^{+0.20}_{-0.06}$	$0.30^{+0.09}_{-0.06}$
XILLVER								
$\log \xi'$	0[a]	0[a]	0[a]	0[a]	0[a]	0[a]	0[a]	0[a]
$N_{\rm XILLVER}$ (10^{-3})	$0.058^{+0.010}_{-0.012}$	$0.080^{+0.016}_{-0.010}$	$0.058^{+0.022}_{-0.023}$	$0.06^{+0.03}_{-0.03}$	$0.058^{+0.011}_{-0.013}$	$0.080^{+0.016}_{-0.017}$	$0.057^{+0.021}_{-0.021}$	$0.06^{+0.04}_{-0.03}$
ZGAUSS								
$E_{\rm line}$ [keV]	$0.808^{+0.016}_{-0.006}$	$0.824^{+0.014}_{-0.010}$	$0.832^{+0.013}_{-0.014}$	$0.821^{+0.015}_{-0.019}$	$0.814^{+0.012}_{-0.012}$	$0.825^{+0.013}_{-0.009}$	$0.831^{+0.014}_{-0.014}$	$0.823^{+0.012}_{-0.024}$
ZGAUSS								
$E_{\rm line}$ [keV]	$1.225^{+0.015}_{-0.021}$	$1.240^{+0.013}_{-0.013}$	$1.246^{+0.007}_{-0.008}$	$1.219^{+0.022}_{-0.016}$	$1.229^{+0.017}_{-0.015}$	$1.241^{+0.012}_{-0.015}$	$1.246^{+0.010}_{-0.011}$	$1.225^{+0.016}_{-0.023}$
χ^2/dof	787.88/737	810.98/685	686.81/640	644.04/594	787.76/737	811.00/685	686.85/640	644.09/594
	$=1.0690$	$=1.1839$	$=1.0731$	$=1.0842$	$=1.0689$	$=1.1839$	$=1.0732$	$=1.0843$
NHP	0.09	0.0006	0.10	0.08	0.10	0.0006	0.10	0.08

Notes. Summary of the best-fit values for model *a* (α_{13} free and $\alpha_{22} = 0$) and model *b* ($\alpha_{13} = 0$ and α_{22} free) for every flux state. The ionization parameter ξ is in units of erg cm s^{-1}. The reported uncertainties correspond to the 90% confidence level for one relevant parameter ($\Delta\chi^2 = 2.71$).
[a] Indicates that the parameter is frozen. NHP is the null hypothesis probability. See the text for more details.

5.1. Comparison with Previous Studies

The best-fit values of α_{13} and α_{22} are very close to 0, so it is relatively straightforward to compare the results obtained here with those from previous studies in which the Kerr background is always assumed.

The studies reported in Brenneman & Reynolds (2006) and Miniutti et al. (2007) are based on less evolved spectral models and the measurements of the parameters of the system are qualitative. Despite that, their results are generically consistent with ours: very high spin parameter a_*, iron abundance higher or much higher than the solar one, inclination angle of the accretion disk in the range of 30°–40°.

A more detailed study of the black hole in MCG–06–30–15 in the Kerr background is reported in Marinucci et al. (2014) analyzing the same *XMM-Newton* and *NuSTAR* observations as our work. For the model parameters that are constant over different flux states, Marinucci et al. (2014) find

$$a_* = 0.91^{+0.06}_{-0.07}, \quad i = 33^\circ \pm 3^\circ,$$
$$A_{\rm Fe} = 1.4 \pm 0.2, \quad \log N_{\rm Fe} = 16.83^{+0.10}_{-0.16}. \tag{9}$$

The estimate of the spin parameter a_* and of the inclination angle of the accretion disk i are consistent with those obtained here. The iron abundance of the accretion disk $A_{\rm Fe}$ and the iron

Table 6
Multi-flux State Analysis

Model	*a*				*b*			
Group	1	2	3	4	1	2	3	4
TBABS								
$N_{\rm H}/10^{22}$ cm^{-2}		0.039[a]				0.039[a]		
WARMABS$_1$								
$N_{\rm H1}/10^{22}$ cm^{-2}	$0.47^{+0.12}_{-0.06}$	$1.163^{+0.015}_{-0.046}$	$0.99^{+0.04}_{-0.03}$	$0.25^{+0.04}_{-0.05}$	$0.46^{+0.22}_{-0.06}$	$1.16^{+0.04}_{-0.09}$	$0.99^{+0.04}_{-0.11}$	$0.25^{+0.09}_{-0.17}$
$\log \xi_1$	$1.86^{+0.04}_{-0.04}$	$1.955^{+0.011}_{-0.020}$	$1.922^{+0.014}_{-0.024}$	$2.48^{+0.09}_{-0.13}$	$1.86^{+0.08}_{-0.10}$	$1.95^{+0.05}_{-0.06}$	$1.92^{+0.03}_{-0.05}$	$2.48^{+0.32}_{-0.18}$
WARMABS$_2$								
$N_{\rm H2}/10^{22}$ cm^{-2}	$0.63^{+0.05}_{-0.06}$	$0.02^{+0.02}_{-0.02}$	$0.54^{+0.17}_{-0.11}$	$0.72^{+0.10}_{-0.04}$	$0.64^{+0.10}_{-0.31}$	$0.02^{+0.02}_{-0.02}$	$0.54^{+0.60}_{-0.23}$	$0.72^{+0.20}_{-0.13}$
$\log \xi_2$	$1.904^{+0.024}_{-0.073}$	$3.09^{+0.09}_{-1.16}$	$3.23^{+0.05}_{-0.06}$	$1.829^{+0.011}_{-0.020}$	$1.90^{+0.11}_{-0.14}$	$3.1_{-1.0}$	$3.23^{+0.13}_{-0.17}$	$1.83^{+0.13}_{-0.04}$
DUSTYABS								
$\log (N_{\rm Fe}/10^{21}$ cm$^{-2})$		$17.411^{+0.006}_{-0.018}$				$17.41^{+0.04}_{-0.05}$		
CUTOFFPL								
Γ	$1.952^{+0.007}_{-0.003}$	$1.971^{+0.006}_{-0.010}$	$2.010^{+0.004}_{-0.011}$	$2.024^{+0.005}_{-0.011}$	$1.952^{+0.018}_{-0.010}$	$1.971^{+0.028}_{-0.013}$	$2.010^{+0.030}_{-0.019}$	$2.024^{+0.025}_{-0.039}$
$E_{\rm cut}$ [keV]	198^{+11}_{-26}	157^{+20}_{-17}	166^{+22}_{-23}	278^{+116}_{-44}	198^{+80}_{-50}	157^{+71}_{-44}	166^{+82}_{-38}	189^{+86}_{-87}
$N_{\rm cutoffpl}$ (10^{-3})	$8.29^{+0.10}_{-0.34}$	$11.94^{+0.20}_{-0.27}$	$14.30^{+0.25}_{-0.33}$	$20.1^{+1.9}_{-1.9}$	$8.3^{+0.6}_{-1.2}$	$12.0^{+2.2}_{-1.1}$	$14.3^{+1.1}_{-0.7}$	$20.1^{+0.5}_{-2.3}$
RELXILL_NK								
$q_{\rm in}$	$6.2^{+1.1}_{-1.0}$	$7.0^{+0.6}_{-0.6}$	$7.68^{+0.36}_{-0.21}$	$8.07^{+0.50}_{-0.17}$	~ 6	$7.0^{+2.8}_{-2.2}$	$7.7^{+0.9}_{-1.1}$	$8.1^{+0.5}_{-2.4}$
$q_{\rm out}$		3[a]				3[a]		
$R_{\rm br}$ [M]	$2.88^{+0.04}_{-0.06}$	$2.98^{+0.14}_{-0.15}$	$3.28^{+0.12}_{-0.06}$	$3.38^{+0.14}_{-0.35}$	$2.88^{+0.17}_{-0.46}$	$3.0^{+0.4}_{-0.9}$	$3.28^{+0.13}_{-0.17}$	$3.4^{+0.8}_{-0.6}$
i [deg]		$31.4^{+1.3}_{-1.4}$				$31.5^{+2.6}_{-2.9}$		
a_*		$0.967^{+0.007}_{-0.013}$				$0.967^{+0.004}_{-0.056}$		
α_{13}		$0.00^{+0.07}_{-0.20}$				0[a]		
α_{22}		0[a]				$0.0^{+0.6}_{-0.1}$		
z		0.007749[a]				0.007749[a]		
$\log \xi$	$2.88^{+0.04}_{-0.06}$	$3.008^{+0.007}_{-0.047}$	$3.064^{+0.020}_{-0.020}$	$3.133^{+0.014}_{-0.021}$	$2.88^{+0.07}_{-0.09}$	$3.008^{+0.025}_{-0.063}$	$3.064^{+0.017}_{-0.022}$	$3.13^{+0.04}_{-0.05}$
$A_{\rm Fe}$		$2.97^{+0.22}_{-0.14}$				$2.98^{+0.49}_{-0.28}$		
$N_{\rm RELXILL\_NK}$ (10^{-3})	$0.125^{+0.012}_{-0.008}$	$0.165^{+0.009}_{-0.007}$	$0.299^{+0.009}_{-0.040}$	$0.383^{+0.010}_{-0.061}$	$0.125^{+0.012}_{-0.024}$	$0.165^{+0.013}_{-0.021}$	$0.300^{+0.158}_{-0.024}$	$0.383^{+0.068}_{-0.015}$
XILLVER								
$\log \xi'$		0[a]				0[a]		
$N_{\rm XILLVER}$ (10^{-3})		$0.058^{+0.004}_{-0.004}$				$0.058^{+0.011}_{-0.010}$		
ZGAUSS								
$E_{\rm line}$ [keV]		$0.8143^{+0.0008}_{-0.0032}$				$0.814^{+0.003}_{-0.003}$		
ZGAUSS								
$E_{\rm line}$ [keV]		$1.226^{+0.011}_{-0.008}$				$1.225^{+0.021}_{-0.020}$		
χ^2/dof		3029.10/2685 = 1.12816				3029.15/2685 = 1.12818		
NHP		$3 \cdot 10^{-6}$				$3 \cdot 10^{-6}$		

Note. Summary of the best-fit values for model *a* (α_{13} free and $\alpha_{22} = 0$) and model *b* ($\alpha_{13} = 0$ and α_{22} free). The ionization parameter ξ is in units of erg cm s^{-1}. The reported uncertainties correspond to the 90% confidence level for one relevant parameter ($\Delta\chi^2 = 2.71$).
[a] Indicates that the parameter is frozen. NHP is the null hypothesis probability. See the text for more details.

column density of the dusty absorber $N_{\rm Fe}$ are somewhat different, but the discrepancy can be easily explained by the different analysis method. The problem of the high iron abundance found in several active galactic nuclei is a well known problem in the literature and presumably due to some systematic uncertainties in the available models. The fact that different analysis methods provide slightly different results can thus be expected as this is a measurement not well under control. Some discrepancy there is indeed even between our single-flux state and multi-flux state analyses. For the model parameters that vary over different flux states, a direct comparison with Marinucci et al. (2014) is not possible because the grouping scheme is different from ours. We just notice that here we find that the ionization parameter of the relativistic reflection component nicely increases with the luminosity, as is expected.

5.2. Constraints on the Kerr Metric

As in our previous studies, our results are consistent with the Kerr black hole hypothesis. The constraint on α_{13} obtained in the present work from MCG–06–30–15 is comparable to that obtained from the stellar-mass black hole in GS 1354–645 (Xu et al. 2018), while the constraint on α_{22} is slightly weaker, see Equations (5) and (6).

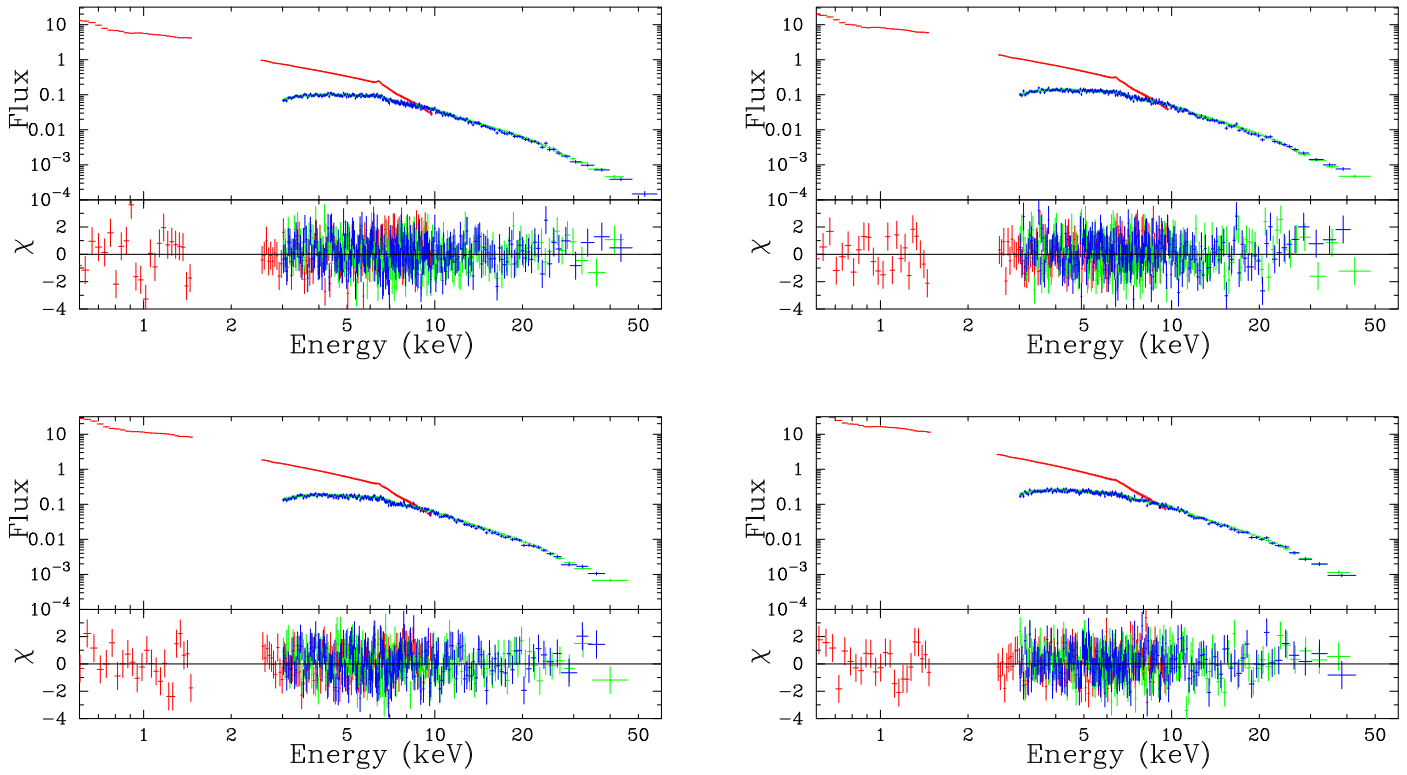

Figure 5. Best-fit model and standard deviations for model a in the multi-flux state analysis. The top left panel is for the low flux state, the top right panel is for the medium flux state, the bottom left panel is for the high flux state, and the bottom right panel is for the very high flux state. Red crosses are used for *XMM-Newton*, green crosses for *NuSTAR*/FPMA, and blue crosses for *NuSTAR*/FPMB.

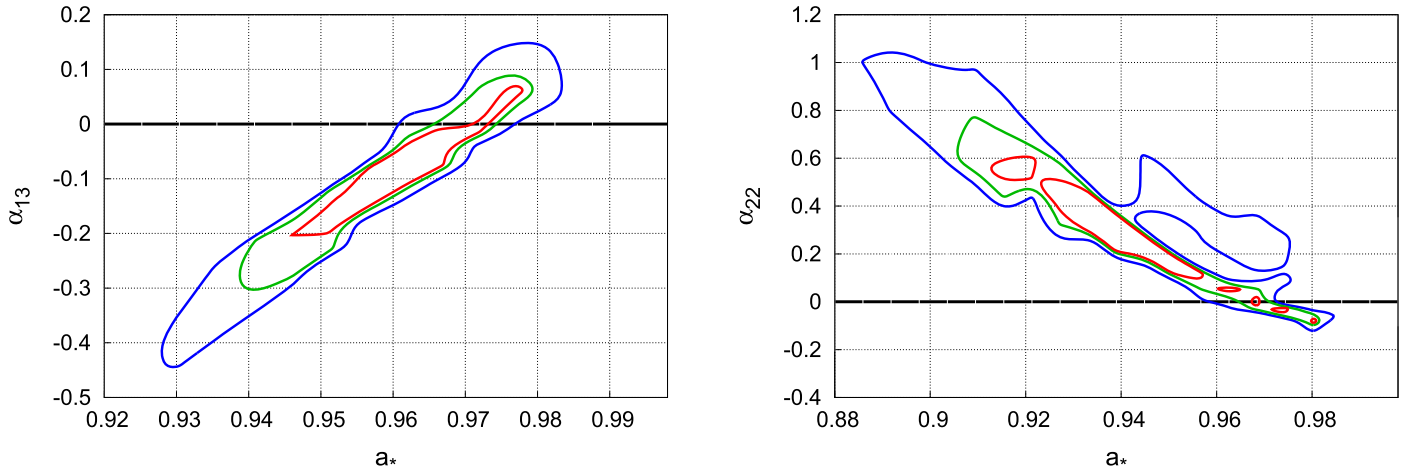

Figure 6. Constraints on the spin parameter a_* and on the Johannsen deformation parameter α_{13} (left panel) and α_{22} (right panel) from the multi-flux state analysis. The red, green, and blue lines indicate, respectively, the 68%, 90%, and 99% confidence level contours for two relevant parameters ($\Delta\chi^2 = 2.30$, 4.61, and 9.21, respectively). The thick black horizontal line marks the Kerr solution.

Table 7
List of the Main Model Simplifications Leading to Systematic Uncertainties

Disk Model	Nonrelativistic Reflection Spectrum
Infinitesimally thin disk	Cold disk
Inner edge at the ISCO	Fixed electron density
No emission inside the ISCO	Constant disk density
Broken power law for emissivity	Solar metallicity except iron
Constant ionization parameter	

Note. They can be grouped into two classes: simplifications in the disk model and those in the calculation of the nonrelativistic spectrum.

On one hand, the fact that we mostly recover the Kerr solution is expected: since Einstein's gravity has already successfully passed a large number of observational tests, it is likely that astrophysical black holes are at least very similar to, if not exactly, the Kerr black holes of Einstein's gravity. On the other hand, since our model has a number of simplifications that inevitably introduce many systematic uncertainties, these confirmations are not at all obvious. The fact that our measurements are consistent with the predictions of Einstein's gravity is surely encouraging. However, in order to be able to perform "precision tests" of general relativity, the systematic uncertainties in our measurements need to be estimated and

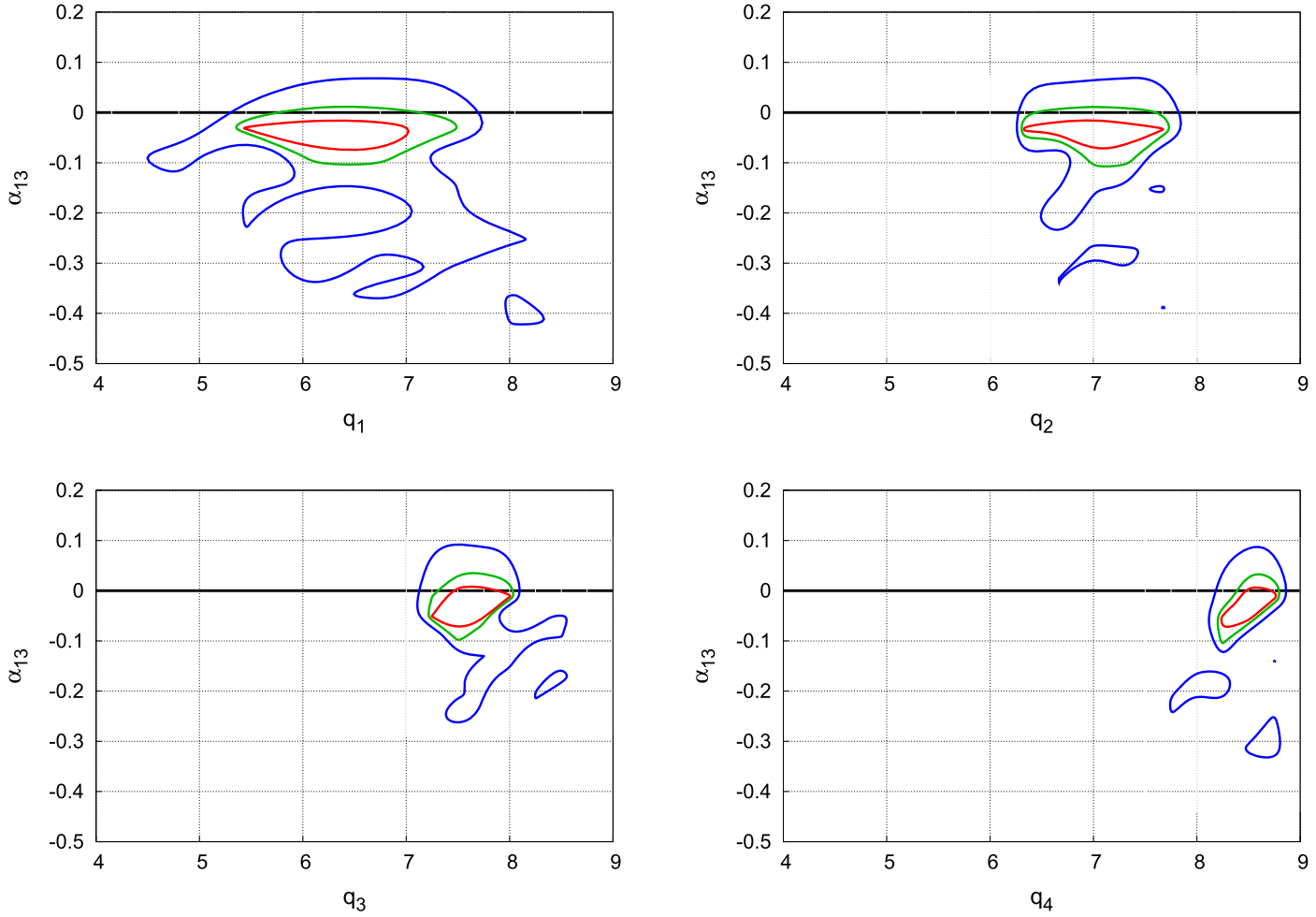

Figure 7. Impact on deformation parameter α_{13} by emissivity profile of different flux intervals. q_1, q_2, q_3, and q_4 are the inner emissivity indices for low, medium, high, and very high flux state, respectively. The red, green, and blue lines indicate, respectively, the 68%, 90%, and 99% confidence level contours for two relevant parameters ($\Delta\chi^2 = 2.30$, 4.61, and 9.21, respectively). The thick black horizontal line marks the Kerr solution.

reduced by employing more sophisticated models. All the uncertainties reported in the present manuscript only refer to the statistical uncertainties. Systematic uncertainties are more difficult to estimate and much more work is necessary.

The systematic (or modeling) uncertainties in the measurements of α_{13} and α_{22} can be grouped into two classes: uncertainties due to the simplified accretion disk model employed and uncertainties in the calculation of the non-relativistic reflection spectrum. Table 7 lists the main contributions.

Disk model. In RELXILL_NK, the accretion disk is assumed to be infinitesimally thin, on the equatorial plane of the black hole, its inner edge is set at the innermost stable circular orbit (ISCO), and no radiation is emitted by the plunging gas between the ISCO and the black hole. In reality, the thickness of the disk is finite and increases with the mass accretion rate. A preliminary study on the impact of the disk thickness on the reflection spectrum has been reported in Taylor & Reynolds (2018). The inner edge of the disk is thought to be at the ISCO radius when the accretion luminosity is between 5% and 30% of the Eddington limit (Penna et al. 2010; Steiner et al. 2010), while for higher luminosities it may move to a smaller radius (Abramowicz & Lasota 1980). For supermassive black holes, it is typically difficult to get reliable estimates of the accretion luminosity, because of the large uncertainties in the estimates of their mass and distance from us. In the case of MCG–06–30–15, the Eddington scaled accretion luminosity has been estimated to be 0.40 ± 0.13 (Brenneman 2013), so deviations from the thin disk model can be expected even if they may be moderate. In reality, some radiation is emitted by the plunging gas, from the ISCO to the black hole.

The emissivity profile is usually thought to be a crucial ingredient and source of systematic uncertainties. To check its impact on the estimate of the deformation parameters, in Xu et al. (2018) we showed that incorrect modeling of the emissivity profile leads to nonvanishing deformation parameters. The fact that we always recover the Kerr metric when we fit the emissivity index suggests that the quality of our data is good enough to permit us to estimate both the deformation parameter and the emissivity index, as an accidental compensation leading to recovery of the Kerr metric sounds unlikely. However, if the emissivity profile is so important for the estimate of the deformation parameter, as suggested in Xu et al. (2018), we should expect that a power law or a broken power law may not be adequate in the case of high quality data, hopefully available with the next generation of X-ray missions (Zhang et al. 2016).

To further explore the role of the emissivity profile on the estimate of the deformation parameters, we have plotted the constraints on the plane $q_{\rm in}$ versus α_{13} for every flux state of the

observations of MCG–6–30–15 studied in this work. Figure 7 shows the 68%, 90%, and 99% confidence level contours for two relevant parameters, where q_1, q_2, q_3, and q_4 are, respectively, the inner emissivity indices for low, medium, high, and very high flux state. These plots do not show any particular correlation between the $q_{\rm in}$ and α_{13}, confirming that the spectral analysis of the source can separately determine these two quantities. Such a conclusion cannot, in general, be extended to any deformation parameter, but at least it seems to hold for α_{13} and α_{22}. Because of the current uncertainties in the corona geometry, and therefore in the exact shape of the emissivity profile, the non-observation of a correlation between the emissivity index and the deformation parameters can partially limit the systematic uncertainty in the estimate of the deformation parameters due to the uncertainty in the correct emissivity profile.

In our accretion disk model, there is a single ionization parameter ξ. In reality, we should expect that ξ is a function of the disk radius, and decreases as we move to larger radii; that is, ξ assumes higher values at the inner edge of the accretion disk, where the temperature of the gas is higher, and decreases at larger radii where the temperature of the disk is lower.

Nonrelativistic reflection spectrum. There are also a number of simplifications in the calculation of the reflection spectrum. XILLVER currently assumes a fixed electron density in the disk, a constant disk density over height and radius, and a disk with solar metallicity with the exception of iron, which is free. These simplifications involve atomic physics only. They affect the prediction of the reflection spectrum at the emission point in the rest-frame of the gas, and they then propagate to the reflection spectrum at the detection point when relativistic effects and the disk model are taken into account.

The problem of the high iron abundance is likely related to systematic uncertainties. This is an issue well known in the literature: the analysis of the reflection spectrum of some sources provides quite high iron abundances, several times the solar value and in some extreme cases even $A_{\rm Fe} \gtrsim 10$. Such a problem can appear in supermassive as well as in stellar-mass black holes; see, e.g., Boller et al. (2002) and García et al. (2015). At the moment, there is no clear explanation for such results: it would be natural to expect $A_{\rm Fe} \sim 1$, lower and higher values may be possible, but very high values of $A_{\rm Fe}$ are presumably unphysical. In specific cases, the problem of the high iron abundance can be solved assuming the existence of two power-law components (Fürst et al. 2015), within a disk wind model (Hagino et al. 2016), or in models with higher disk electron densities (Tomsick et al. 2018), but none of these explanations is completely satisfactory. Such a problem questions the accuracy of the parameter estimates, and in our case of the possibility of testing general relativity. Since we currently do not know the origin of such high values of $A_{\rm Fe}$, it is not possible to answer the question about the accuracy of the parameter estimates, but it is surely an issue to solve if we want to use X-ray reflection spectroscopy for precision measurements of the spacetime metric around black holes.

At the moment, a systematic study on the impact of all these simplifications on the measurements of the spin and the deformation parameters is lacking, but work is underway. An estimate of the systematic uncertainty from every effect can be obtained by constructing a model that takes the effect into account and then by studying its impact on the final measurement, either with simulated or real data, or with both. In the end, the possibility of performing precision tests of general relativity using black hole X-ray reflection spectroscopy will be determined by our capability of modeling these systems in order to make the systematic uncertainties subdominant with respect to the statistical ones.

A.T. thanks Laura Brenneman for useful discussions on MCG–06–30–15. This work was supported by the National Natural Science Foundation of China (NSFC), grant No. U1531117, and Fudan University, grant No. IDH1512060. A.T. also acknowledges support from the China Scholarship Council (CSC), grant No. 2016GXZR89. S.N. acknowledges support from the Excellence Initiative at Eberhard-Karls Universität Tübingen. A.B.A. also acknowledges the support from the Shanghai Government Scholarship (SGS). J.A.G. acknowledges support from the Alexander von Humboldt Foundation.

ORCID iDs

Ashutosh Tripathi https://orcid.org/0000-0002-3960-5870
Cosimo Bambi https://orcid.org/0000-0002-3180-9502

References

Abramowicz, M. A., & Lasota, J. P. 1980, AcA, 30, 35
Bambi, C. 2012a, PhRvD, 85, 043001
Bambi, C. 2012b, PhRvD, 86, 123013
Bambi, C. 2012c, ApJ, 761, 174
Bambi, C. 2013, PhRvD, 87, 023007
Bambi, C. 2017, RvMP, 89, 025001
Bambi, C. 2018, AnP, 530, 1700430
Bambi, C., Abdikamalov, A., Ayzenberg, D., et al. 2018, Univ, 4, 79
Bambi, C., Cárdenas-Avendaño, A., Dauser, T., García, J. A., & Nampalliwar, S. 2017, ApJ, 842, 76
Bambi, C., Jiang, J., & Steiner, J. F. 2016, CQGra, 33, 064001
Boller, T., Fabian, A. C., Sunyaev, R., et al. 2002, MNRAS, 329, L1
Brenneman, L. 2013, Measuring the Angular Momentum of Supermassive Black Holes (Berlin: SpringerBriefs)
Brenneman, L. W., & Reynolds, C. S. 2006, ApJ, 652, 1028
Cao, Z., Nampalliwar, S., Bambi, C., Dauser, T., & García, J. A. 2018, PhRvL, 120, 051101
Cardoso, V., & Gualtieri, L. 2016, CQGra, 33, 174001
Carter, B. 1971, PhRvL, 26, 331
Choudhury, K., Nampalliwar, S., Abdikamalov, A. B., et al. 2018, arXiv:1809.06669
Chruściel, P. T., Costa, J. L., & Heusler, M. 2012, LRR, 15, 7
Dauser, T., Garcia, J., Wilms, J., et al. 2013, MNRAS, 430, 1694
Dickey, J. M., & Lockman, F. J. 1990, ARA&A, 28, 215
Fabian, A. C., Vaughan, S., Nandra, K., et al. 2002, MNRAS, 335, L1
Fürst, F., Nowak, M. A., Tomsick, J. A., et al. 2015, ApJ, 808, 122
García, J., Dauser, T., Lohfink, A., et al. 2014, ApJ, 782, 76
García, J., Dauser, T., Reynolds, C. S., et al. 2013, ApJ, 768, 146
García, J., & Kallman, T. R. 2010, ApJ, 718, 695
García, J., Kallman, T. R., & Mushotzky, R. F. 2011, ApJ, 731, 131
García, J. A., Steiner, J. F., McClintock, J. E., et al. 2015, ApJ, 813, 84
George, I. M., & Fabian, A. C. 1991, MNRAS, 249, 352
Guainazzi, M., Matt, G., Molendi, S., et al. 1999, A&A, 341, L27
Hagino, K., Odaka, H., Done, C., et al. 2016, MNRAS, 461, 3954
Harrison, F. A., Craig, W. W., Christensen, F. E., et al. 2013, ApJ, 770, 103
Hoormann, J. K., Beheshtipour, B., & Krawczynski, H. 2016, PhRvD, 93, 044020
Iwasawa, K., Fabian, A. C., Reynolds, C. S., et al. 1996, MNRAS, 282, 1038
Jansen, F., Lumb, D., Altieri, B., et al. 2001, A&A, 365, L1
Johannsen, T. 2013, PhRvD, 88, 044002
Johannsen, T. 2016, CQGra, 33, 124001
Johannsen, T., & Psaltis, D. 2011, ApJ, 726, 11
Johannsen, T., & Psaltis, D. 2013, ApJ, 773, 57
Kong, L., Li, Z., & Bambi, C. 2014, ApJ, 797, 78
Krawczynski, H. 2012, ApJ, 754, 133
Krawczynski, H. 2018, GReGr, 50, 100

Lee, J. C., Fabian, A. C., Reynolds, C. S., Brandt, W. N., & Iwasawa, K. 2000, MNRAS, 318, 857
Lee, J. C., Ogle, P. M., Canizares, C. R., et al. 2001, ApJL, 554, L13
Leighly, K. M., Mushotzky, R. F., Nandra, K., & Forster, K. 1997, ApJL, 489, L25
Marinucci, A., Matt, G., Miniutti, G., et al. 2014, ApJ, 787, 83
Miller, L., Turner, T. J., & Reeves, J. N. 2008, A&A, 483, 437
Miniutti, G., Fabian, A. C., Anabuki, N., et al. 2007, PASJ, 59, 315
Penna, R. F., McKinney, J. C., Narayan, R., et al. 2010, MNRAS, 408, 752
Robinson, D. C. 1975, PhRvL, 34, 905
Ross, R. R., & Fabian, A. C. 2005, MNRAS, 358, 211
Sako, M., Kahn, S. M., Branduardi-Raymont, G., et al. 2003, ApJ, 596, 114
Steiner, J. F., McClintock, J. E., Remillard, R. A., et al. 2010, ApJL, 718, L117
Strüder, L., Briel, U., Dennerl, K., et al. 2001, A&A, 365, L18
Tanaka, Y., Nandra, K., Fabian, A. C., et al. 1995, Natur, 375, 659
Taylor, C., & Reynolds, C. S. 2018, ApJ, 855, 120
Tomsick, J. A., Parker, M. L., García, J. A., et al. 2018, ApJ, 855, 3
Tripathi, A., Nampalliwar, S., Abdikamalov, A. B., et al. 2018, PhRvD, 98, 023018
Wang-Ji, J., Abdikamalov, A. B., Ayzenberg, D., et al. 2018, arXiv:1806.00126
Will, C. M. 2014, LRR, 17, 4
Wilms, J., Reynolds, C. S., Begelman, M. C., et al. 2001, MNRAS, 328, L27
Xu, Y., Nampalliwar, S., Abdikamalov, A. B., et al. 2018, ApJ, 865, 134
Yagi, K., & Stein, L. C. 2016, CQGra, 33, 054001
Zhang, S. N., Feroci, M., Santangelo, A., et al. 2016, Proc. SPIE, 9905, 99051Q